

# Waveform Learning for Next-Generation Wireless Communication Systems

Fayçal Ait Aoudia, *Member, IEEE*, and Jakob Hoydis, *Senior Member, IEEE*

## Abstract

We propose a learning-based method for the joint design of a transmit and receive filter, the constellation geometry and associated bit labeling, as well as a neural network (NN)-based detector. The method maximizes an achievable information rate, while simultaneously satisfying constraints on the adjacent channel leakage ratio (ACLR) and peak-to-average power ratio (PAPR). This allows control of the tradeoff between spectral containment, peak power, and communication rate. Evaluation on an additive white Gaussian noise (AWGN) channel shows significant reduction of ACLR and PAPR compared to a conventional baseline relying on quadrature amplitude modulation (QAM) and root-raised-cosine (RRC), without significant loss of information rate. When considering a 3rd Generation Partnership Project (3GPP) multipath channel, the learned waveform and neural receiver enable competitive or higher rates than an orthogonal frequency division multiplexing (OFDM) baseline, while reducing the ACLR by 10 dB and the PAPR by 2 dB. The proposed method incurs no additional complexity on the transmitter side and might be an attractive tool for waveform design of beyond-5G systems.

## Index Terms

Pulse shaping, Geometric shaping, Autoencoder, Deep learning, Waveform learning

## I. INTRODUCTION

Orthogonal frequency division multiplexing (OFDM) is the dominant waveform in current wireless communication systems, such as 4G, 5G, and WiFi, because it allows for a very efficient hardware implementation as well as single-tap equalization. However, its sensitivity to frequency dispersion, reduction of spectral efficiency due to the cyclic prefix and guard bands, as well as

F. Ait Aoudia and J. Hoydis are with NVIDIA, 06906 Sophia Antipolis, France (faitaoudia@nvidia.com, jhoydis@nvidia.com). Work carried out while both authors were with Nokia Bell Labs, France.

Parts of this work have been published in [1].

high peak-to-average power ratio (PAPR) and adjacent channel leakage ratio (ACLR) make it unsuitable for future radio systems which are supposed to operate at very high carrier frequencies and as energy-efficiently as possible. For example, the low power amplifier efficiency in the sub-THz bands calls for low PAPR waveforms that are able to deal with high phase noise while meeting strict requirements on out-of-band emissions [2]. Moreover, the increased range of applications foreseen for beyond-5G systems could lead to a much wider range of waveforms available in future standards to efficiently fit the numerous edge cases, such as massive access from IoT devices in private industrial networks. Many waveforms have been introduced to address some of the drawbacks of OFDM, such as orthogonal time frequency and space (OTFS) [3] and generalized frequency division multiplexing (GFDM) [4]. Also signal processing techniques on-top-of OFDM were proposed to reduce its PAPR and ACLR, such as the use of guard subcarriers to improve spectral containment, and the allocation of pilot reduction tones (PRTs) to reduce power peaks [5], [6]. However, they require significant additional complexity on the transmitter side, and incur a rate loss as the subcarriers used as guards or PRTs do not carry data.

Recent work has demonstrated the competitiveness of neural receivers for conventional waveforms [7]–[9]. However, such receivers can be trained to demodulate in principle *any* waveform carrying information. Thus, they open the door to novel waveforms which cannot be easily demodulated by conventional techniques. Building on this idea, we propose in this work to use end-to-end learning to jointly design a transmit and receive filter, a constellation geometry and the corresponding bit labeling, as well as a neural receiver. The key idea of end-to-end learning [10] is to implement the transmitter, channel, and receiver as a neural network (NN), that is trained to maximize an achievable information rate. On the transmitter side, the widely-used bit-interleaved coded modulation (BICM) architecture [11] is preserved, such that no additional complexity is introduced compared to conventional systems. This has the additional benefit that an outer error-correcting code can be used. On the receiver side, the neural receiver computes log-likelihood ratios (LLRs) for the transmitted bits directly from the received samples. Optimization of the end-to-end system is performed to maximize the practical bit-metric decoding (BMD) rate with constraints on the ACLR and PAPR of the waveform used for transmission.

The end-to-end learning approach was evaluated on both an additive white Gaussian noise (AWGN) and a 3rd Generation Partnership Project (3GPP) multipath channel. Results show that the proposed approach enables fine control of the tradeoff between the achievable information rate, ACLR, and PAPR. On an AWGN channel, a single-carrier waveform using quadrature

amplitude modulation (QAM), root-raised-cosine (RRC) filtering, and Blackman windowing was used as benchmark. The learning-based approach enables up to 30 dB lower ACLR compared to the baseline, while achieving a similar PAPR and competitive rate. Significant reduction of the PAPR can also be achieved, however at the cost of a rate loss. A multiple access channel involving two interfering users transmitting to a single receiver was also considered: two users share the same band, but each has their own trainable constellation and transmit filter. The learned system enables rates greater than the ones achieved with QAM, a BMD receiver, and orthogonal multiple access (OMA), by learning distinguishable constellations and transmit filters. When considering a single-user 3GPP multipath channel, OFDM with QAM was used for benchmarking, with linear minimum mean square error (LMMSE) channel estimation and single-tap equalization. Simulation results show that the learned waveform achieves similar or higher information rates than the considered baseline, while enabling 10 dB lower ACLRs, and 2 dB lower PAPRs.

The rest of this paper is organized as follows. Section II presents the related work. Section III introduces the system model, and Section IV formulates the problem we aim to solve. Section V presents the end-to-end learning approach, and Section VI the results of our simulations. Finally, Section VII concludes the paper.

*Notations:* Boldface upper-case (lower-case) letters denote matrices (column vectors); regular lower-case letters denote scalars.  $\mathbb{R}$  ( $\mathbb{C}$ ) is the set of real (complex) numbers;  $(\cdot)^*$  is the complex conjugate operator.  $\log_2(\cdot)$  denotes the binary logarithm. The  $(i, k)$  element of a matrix  $\mathbf{X}$  is denoted by  $X_{i,k}$ . The  $k^{\text{th}}$  element of a vector  $\mathbf{x}$  is  $x_k$ . The operators  $(\cdot)^H$  and  $(\cdot)^T$  denote the Hermitian transpose and transpose, respectively. Finally,  $j = \sqrt{-1}$  denotes the imaginary unit.

## II. RELATED WORK

The drawbacks of OFDM have led to the introduction of many alternatives such as OTFS [3], whose key idea is to perform modulation in the delay-Doppler domain instead of the time-frequency domain, making it more robust to frequency dispersion. Another example is GFDM [4] which turns the channel into multiple parallel, independent, and possibly interfering single-carrier links. Other examples of waveform proposals are available in [12] and references therein. Concerning OFDM, its high PAPR and ACLR are not novel concerns, see, e.g., [6]. In [5], the authors propose to reserve subcarriers to the transmission of peak-canceling signals (PRTs). With this method, PAPR reduction can only be achieved at the cost of a rate loss, as the subcarriers allocated to PRTs do not carry data. Moreover, the optimal PRTs depend on the transmitted

baseband symbols. This implies that an iterative and computationally demanding algorithm needs to be run for each OFDM symbol, making this approach unpractical. In [13], the authors have extended the tone reduction method by unfolding a conventional algorithm to an NN, which is trained offline to predict the PRTs from the data symbols. A similar approach was followed in [14]. The authors of [15] use a non model-based approach to predict the PRTs from the data symbols with the help of an NN. Still focusing on PAPR reduction of OFDM, it is proposed in [16] to extend the outer points of QAM constellations with an active extension method. As for PRTs, the computation of the constellation extension needs to be carried out by an iterative and computationally demanding algorithm for each OFDM symbol. To address this issue, [17] proposes to use an NN to compute the constellation extension from the data symbols.

A different line of works consist in learning possibly high-dimensional modulations that operate on top of existing waveforms, typically OFDM. This approach was applied, e.g., in [18], [19] to achieve pilotless and cyclic prefix (CP)-less communication, or in [20] to improve the bit error rate (BER). However, these works do not consider the PAPR or ACLR. In [21], the authors use an NN to perform high dimensional modulation and demodulation on top of OFDM, with the aim to improve the PAPR while achieving low BERs. However, only the non-oversampled transmitted signal is used for the PAPR computation, which is not completely representative of the analog waveform that actually serves as input to the power amplifier. Moreover, the ACLR is not taken into account. More recently, end-to-end learning of a high dimensional modulation and demodulation scheme operating on top of OFDM was proposed in [22]. Here, the transmitter and receiver were jointly optimized to maximize an achievable rate under predefined constraints on the PAPR and ACLR. In the field of optical communications, end-to-end learning was used to improve the PAPR [23], [24] and ACLR [25] of existing waveforms.

All of the references cited above propose methods operating on top of existing waveforms, such as OFDM. In this work, we present a method to design a novel single-carrier waveform by jointly optimizing the transmit filter and constellation geometry to maximize an achievable information rate while satisfying constraints on the PAPR and ACLR. Compared to previous work, our approach does not require an NN at the transmitter side and preserves the architecture and complexity of a conventional single-carrier system. Moreover, by suitably designing the neural receiver, higher rates than those achieved by OFDM are obtained on multipath channels, while preserving the benefits of the learned single-carrier waveform, i.e., low ACLR and PAPR.

### III. SYSTEM MODEL

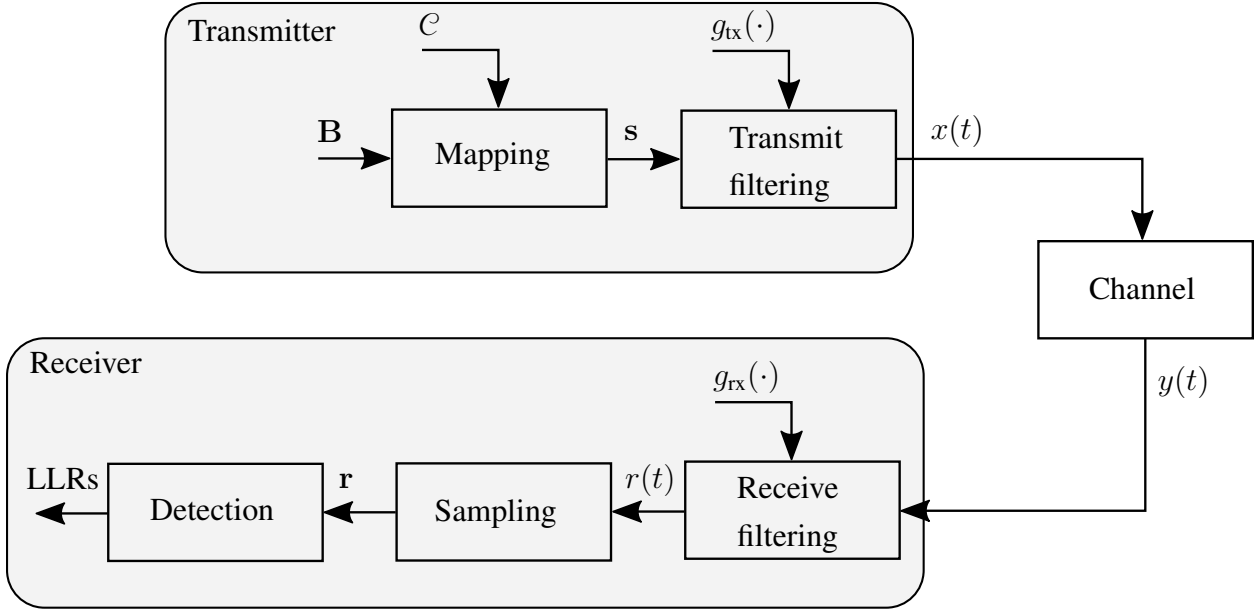


Fig. 1: Architecture of a single-carrier system, where  $\mathcal{C}$  is the constellation used for mapping,  $g_{tx}(\cdot)$  the transmit filter, and  $g_{rx}(\cdot)$  the receive filter.

Let us denote by  $\mathbf{B} \in \{0, 1\}^{N \times K}$  the matrix of bits in a transmit block which consists of  $N$  baseband symbols carrying each  $K$  bits. We consider BICM, where  $\mathbf{B}$  is modulated onto a vector of baseband symbols  $\mathbf{s} \in \mathcal{C}^N$  according to a constellation  $\mathcal{C} \in \mathbb{C}^{2^K}$  and a corresponding bit labeling, e.g., a  $2^K$ -QAM with Gray labeling, or a learned constellation geometry and labeling. We assume a classic single-carrier scheme in which the modulated symbols are shaped with a transmit filter  $g_{tx} : t \in \mathbb{R} \rightarrow \mathbb{C}$  to form the time-continuous baseband signal

$$x(t) = \sum_{n=0}^{N-1} s_n g_{tx}(t - nT) \quad (1)$$

where  $T$  is the symbol period. This process is illustrated in Fig. 1.

We consider a time-invariant multipath channel with baseband-equivalent transfer function

$$h(\tau) = \sum_{p=0}^{P-1} a_p \delta(\tau - \tau_p) \quad (2)$$

where  $\delta(\cdot)$  is the Dirac delta function,  $P$  is the number of paths, and  $a_p$  and  $\tau_p$  are the complex baseband channel coefficient and delay of the  $p^{th}$  path, respectively. The time-continuous channel output is given by

$$y(t) = \int h(\tau)x(t-\tau)d\tau + w(t) = \sum_{n=0}^{N-1} s_n \sum_{p=0}^{P-1} a_p g_{\text{tx}}(t - \tau_p - nT) + w(t) \quad (3)$$

where  $w(t)$  is uncorrelated Gaussian noise with power spectral density  $N_0$ , satisfying the condition  $\mathbb{E}[w(t)w(t+\tau)^*] = N_0\delta(\tau)$ .

At the receiver,  $y(t)$  is first filtered using a receive filter  $g_{\text{rx}} : t \in \mathbb{R} \rightarrow \mathbb{C}$ , leading to

$$r(t) = \int y(z)g_{\text{rx}}^*(t-z)dz \quad (4)$$

$$= \sum_{n=0}^{N-1} s_n \sum_{p=0}^{P-1} a_p \int g_{\text{tx}}(z')g_{\text{rx}}^*(t - z' - \tau_p - nT) dz' + \int w(z)g_{\text{rx}}(t-z)dz \quad (5)$$

where the second equality comes from introducing  $z' := z - \tau_p - nT$ . The filtered received signal is then sampled with a period  $T$  to form the vector  $\mathbf{r} \in \mathbb{C}^N$  with elements

$$r_m = r(mT) = \sum_{\ell} s_{m-\ell} h_{\ell} + w_m \quad (6)$$

where  $\ell := m - n$  and the channel taps  $h_{\ell}$  are given by

$$h_{\ell} = \sum_{p=0}^{P-1} a_p (g_{\text{tx}} * g_{\text{rx}}^*)(\ell T - \tau_p) \quad (7)$$

where  $*$  denotes the convolution operation and  $n_m$  is additive Gaussian noise with correlation

$$\mathbb{E}[w_m w_{m+\ell}^*] = N_0 \int g_{\text{rx}}^*(t)g_{\text{rx}}(t + \ell T) dt. \quad (8)$$

As illustrated in Fig. 1,  $\mathbf{r}$  is processed by a detector which computes LLRs on the transmitted bits, which could then be fed to an outer decoder.

### QAM with RRC filtering

As a baseline for comparison on the AWGN channel, we consider the widely used QAM with Gray labeling and RRC filtering. The RRC filter is denoted by  $\text{rrc}_{\beta}(t)$ , where  $\beta \in (0, 1)$  is the roll-off factor which controls the tradeoff between the excess bandwidth and the magnitude of the ripples. When used with its match filter  $\text{rrc}_{\beta}(-t) = \text{rrc}_{\beta}(t)$ , the RRC filter satisfies the Nyquist inter-symbol interference (ISI) criterion [26, Chapter 9.2.1]

$$(\text{rrc}_{\beta} * \text{rrc}_{\beta})(\ell T) = \begin{cases} 1 & \text{if } \ell = 0 \\ 0 & \text{otherwise} \end{cases} \quad (9)$$

where  $\ell \in \mathbb{Z}$ . Because the RRC filter is not time-limited, it is windowed by the Blackman windowing function  $\text{bm}(t)$ , which results in the following transmit and receive filters:

$$g_{\text{tx}}(t) = g_{\text{rx}}(t) = \text{rrc}_{\beta}(t)\text{bm}\left(\frac{t}{D}\right) \quad (10)$$

where  $D > 0$  is the filter duration.

#### IV. PROBLEM STATEMENT

We will now present the optimization problem that we seek to address through end-to-end learning in Section V. As shown in Fig. 1, we consider a single-carrier system, where the transmit and receive filters, denoted respectively by  $g_{\text{tx},\theta}(\cdot)$  and  $g_{\text{rx},\psi}(\cdot)$ , have trainable parameters  $\theta$  and  $\psi$ . Both filters are limited to the interval  $(-\frac{D}{2}, \frac{D}{2})$ , i.e., for  $t \notin (-\frac{D}{2}, \frac{D}{2})$ ,  $g_{\text{tx},\theta}(t) = g_{\text{rx},\psi}(t) = 0$ . On the transmitter side, the constellation geometry  $\mathcal{C}$  and corresponding bit labeling are also trainable. On the receiver side, the detector is implemented by a neural receiver with trainable parameters  $\gamma$ , which computes a posterior distribution  $Q_{\gamma}(B_{n,k}|\mathbf{r})$ ,  $0 \leq n \leq N-1$ ,  $0 \leq k \leq K-1$ , or equivalently LLRs, on the transmitted bits  $B_{n,k}$  from the received samples  $\mathbf{r}$ .

Most practical systems rely on BICM and BMD for which the information rate

$$R(\mathcal{C}, \theta, \psi, \gamma) := \frac{1}{N} \sum_{n=0}^{N-1} \sum_{k=0}^{K-1} I(B_{n,k}; \mathbf{r} | \mathcal{C}, \theta, \psi) - \mathbb{E}_{\mathbf{r}} [\text{D}_{\text{KL}}(\text{Pr}(B_{n,k}|\mathbf{r}) || Q_{\gamma}(B_{n,k}|\mathbf{r}))] \quad (11)$$

is known to be an achievable rate [27]. Therefore, we aim to maximize this rate. Note that maximizing this rate typically leads to very different results than when maximizing the more conventional symbol-wise mutual information [28], which is known to not be an achievable rate for practical BMD receivers. Moreover, using the BMD rate (11) as objective enables joint optimization of the constellation geometry and bit labeling. In (11),  $I(B_{n,k}; \mathbf{r} | \mathcal{C}, \theta, \psi)$  is the mutual information between  $B_{n,k}$  and  $\mathbf{r}$  conditioned on the constellation and filters,  $\text{D}_{\text{KL}}(\cdot || \cdot)$  is the Kullback–Leibler (KL) divergence, and  $\text{Pr}(B_{n,k}|\mathbf{r})$  is the *true* posterior distribution on  $B_{n,k}$  given  $\mathbf{r}$ . Intuitively, the first term on the right-hand side of (11) corresponds to an achievable rate assuming an optimal BMD receiver, i.e., one that implements  $\text{Pr}(B_{n,k}|\mathbf{r})$ . The second term is the rate loss due to the use of a mismatched receiver, i.e.,  $Q_{\gamma}(B_{n,k}|\mathbf{r}) \neq \text{Pr}(B_{n,k}|\mathbf{r})$ .

For practical purposes, the maximization of (11) must be done under constraints on the transmitted waveform. First, the transmit filter and constellation must have unit energy, i.e.,

$$\int_{-\frac{D}{2}}^{\frac{D}{2}} |g_{\text{tx},\theta}(t)|^2 dt = 1 \quad (12)$$

$$\mathbb{E}_{c \sim \mathcal{U}(\mathcal{C})} [|c|^2] = 1 \quad (13)$$

where  $\mathcal{U}(\mathcal{C})$  is the uniform distribution on  $\mathcal{C}$ .

Concerning the power spectral density (PSD), the ACLR is defined as

$$\text{ACLR}(\theta) := \frac{E_O(\theta)}{E_I(\theta)} = \frac{1}{E_I(\theta)} - 1 \quad (14)$$

where  $E_I(\theta)$  and  $E_O(\theta)$  are the in- and out-of-band energy, respectively, and the second equality comes from (12) since  $E_I(\theta) + E_O(\theta) = 1$ . As we consider BICM, the sequence of modulated symbols  $\mathbf{s}$  is independent and identically distributed (i.i.d.), so that the in-band energy is

$$E_I(\theta) = \int_{-\frac{W}{2}}^{\frac{W}{2}} |\hat{g}_{\text{tx},\theta}(f)|^2 df \quad (15)$$

where  $W := \frac{1}{T}$  is the bandwidth and  $\hat{g}_{\text{tx},\theta}(f)$  the Fourier transform of  $g_{\text{tx},\theta}(t)$ .

With regards to the power envelope, we denote by  $p(t) := |x(t)|^2$  the signal power at time  $t$ . Note that at every instant  $t$ ,  $p(t)$  is a random variable because of the randomness of the baseband symbols  $\mathbf{s}$ . Since the sequence of baseband symbols  $\mathbf{s}$  is i.i.d.,  $p(t)$  and  $p(t + \ell T)$  share the same distribution for any  $\ell \in \mathbb{Z}$  and  $t$ , such that  $t$  and  $t + \ell T$  are at least  $\frac{D}{2}$  away from the temporal edges of the signal. This can be seen from the definition of the transmitted signal (1). Therefore, it is sufficient to consider a single period  $(-\frac{T}{2}, \frac{T}{2})$ . The PAPR is defined as

$$\text{PAPR}(\theta, \mathcal{C}) := \min_{\nu \geq 0} \nu \quad (16a)$$

$$\text{subject to } \Pr \left( \frac{p(t)}{\bar{p}} > \nu \right) = 0, \forall t \in \left( -\frac{T}{2}, \frac{T}{2} \right) \quad (16b)$$

where

$$\bar{p} = \frac{N}{(N-1)T + D} \quad (17)$$

is the average signal power. One can notice that the equality (16b) is equivalent to

$$\mathbb{E} \left[ \max \left( \frac{p(t)}{\bar{p}} - \nu, 0 \right) \right] = 0 \quad (18)$$

where the expectation is over  $\mathbf{s}$  and  $t \sim \mathcal{U}(-\frac{T}{2}, \frac{T}{2})$ .

Maximizing (11) with constraints on the ACLR and PAPR leads to the following optimization problem that we aim to solve

$$\underset{\mathcal{C}, \boldsymbol{\theta}, \boldsymbol{\psi}, \boldsymbol{\gamma}}{\text{maximize}} \quad R(\mathcal{C}, \boldsymbol{\theta}, \boldsymbol{\psi}, \boldsymbol{\gamma}) \quad (19a)$$

$$\text{subject to} \quad \int_{-\frac{D}{2}}^{\frac{D}{2}} |g_{\text{tx}, \boldsymbol{\theta}}(t)|^2 dt = 1 \quad (19b)$$

$$\mathbb{E}_{c \sim \mathcal{U}(\mathcal{C})} [|c|^2] = 1 \quad (19c)$$

$$\text{ACLR}(\boldsymbol{\theta}) \leq \epsilon_A \quad (19d)$$

$$\text{PAPR}(\boldsymbol{\theta}, \mathcal{C}) \leq \epsilon_P \quad (19e)$$

where (19b) and (19c) constrain the energy of the transmit filter and constellation, respectively, and (19d) and (19e) enforce the ACLR and PAPR to be less than or equal to  $\epsilon_A$  and  $\epsilon_P$ , respectively. From (16a), (16b), and (18), one can see that the constraint (19e) is equivalent to

$$V(\boldsymbol{\theta}, \mathcal{C}, \epsilon_P) := \mathbb{E} \left[ \max \left( \frac{p(t)}{\bar{p}} - \epsilon_P, 0 \right) \right] = 0 \quad (20)$$

where the expectation is over  $\mathbf{s}$  and  $t \sim \mathcal{U}(-\frac{T}{2}, \frac{T}{2})$ .

## V. END-TO-END WAVEFORM LEARNING

End-to-end learning consists in implementing the transmitter, channel, and receiver as an NN that is trained using stochastic gradient descent (SGD) by backpropagating the gradient from the receiver to the transmitter through the channel. The considered end-to-end system is shown in Fig. 2, where the trainable components appear in light gray. The channel is simulated in the discrete-time domain by implementing the transfer function (6), which involves evaluating the channel taps (7) and noise correlation (8). The transmit and receive filters affect the received samples  $\mathbf{r}$  through the channel taps and noise correlation. Training of the system through SGD requires efficient computation of the channel taps and noise correlation. These computations must also be differentiable. This is made challenging as (7) and (8) involve integration. The way how we solve this problem is detailed in Section V-A. Section V-B presents the implementation of the trainable constellation, and Section V-C the neural receiver architecture. Finally, in Section V-D, we explain entire the training process.

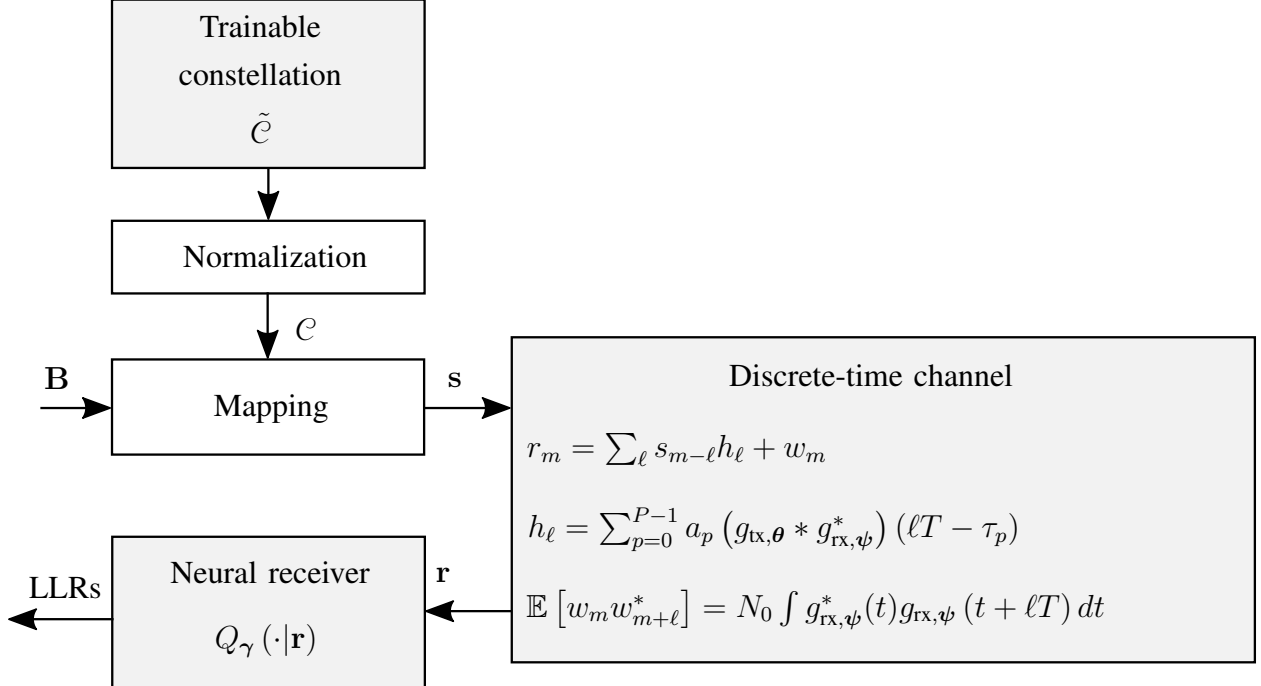


Fig. 2: The trainable end-to-end system is implemented using a discrete-time channel model, which includes the effects of the transmit and receive filters. Components that include trainable parameters are shown in light gray.

#### A. Trainable transmit and receive filters

As the computations of the channel taps (7) and noise correlation (8) require integration, we cannot easily use NNs to implement the transmit and receiver filters as it would lead to intractable calculations. One could, e.g., approximate the integrals using Monte Carlo estimation or Riemann sums, but this is computationally demanding. To accurately and efficiently implement trainable transmit and receive filters, we use the fact that the functions  $\{\text{sinc}(Df - s)\}_{s \in \mathbb{Z}}$  form a frequency-domain basis of functions which are time-limited to  $(-\frac{D}{2}, \frac{D}{2})$ . We therefore define the trainable transmit and receive filters in the frequency domain as

$$\hat{g}_{\text{tx},\theta}(f) := \sqrt{C(\theta)} \sum_{s=-S}^S \theta_s \text{sinc}(Df - s) \quad (21)$$

$$\hat{g}_{\text{rx},\psi}(f) := \sum_{s=-S}^S \psi_s \text{sinc}(Df - s) \quad (22)$$

where  $S$  controls the number of trainable parameters. The trainable parameters of the transmit and receiver filters are  $\theta = [\theta_{-S}, \dots, 0, \dots, \theta_S]^T$  and  $\psi = [\psi_{-S}, \dots, 0, \dots, \psi_S]^T$ , respectively.

Note that both filters are neither required to have the same number of parameters  $2S + 1$  nor the same duration  $D$ . In (21),  $C(\boldsymbol{\theta})$  is a normalization constant that ensures that the transmit filter has unit energy (19b). Taking the inverse Fourier transform of (21) and (22) leads to the time-domain expressions of the trainable filters

$$g_{\text{tx},\boldsymbol{\theta}}(t) = \frac{\sqrt{C(\boldsymbol{\theta})}}{D} \text{rect}\left(\frac{t}{D}\right) \sum_{s=-S}^S \theta_s e^{j2\pi\frac{s}{D}t} \quad (23)$$

$$g_{\text{rx},\boldsymbol{\psi}}(t) = \frac{1}{D} \text{rect}\left(\frac{t}{D}\right) \sum_{s=-S}^S \psi_s e^{j2\pi\frac{s}{D}t}. \quad (24)$$

One can see from these equations, that the transmit and receive filters are defined through Fourier series with  $2S + 1$  harmonics and period  $D$ , which are time-limited to a single period.

By using this filter parametrization, all of the quantities required to simulate the discrete-time channel have closed-form expressions that can be easily evaluated numerically:

$$C(\boldsymbol{\theta}) = \frac{D}{\boldsymbol{\theta}^H \boldsymbol{\theta}} \quad (25)$$

$$(g_{\text{tx},\boldsymbol{\theta}} * g_{\text{tx},\boldsymbol{\psi}}^*)(t) = \begin{cases} \frac{\sqrt{C(\boldsymbol{\theta})}}{D} \boldsymbol{\psi}^H \mathbf{A}(t) \boldsymbol{\theta} & \text{if } t \in (-D, D) \\ 0 & \text{otherwise} \end{cases} \quad (26)$$

$$\mathbb{E} [w_m w_{m+\ell}^*] = \begin{cases} \frac{N_0}{D} \boldsymbol{\psi}^H \mathbf{A}'(\ell T) \boldsymbol{\psi} & \text{if } \ell T \in (-D, D) \\ 0 & \text{otherwise} \end{cases} \quad (27)$$

where  $\mathbf{A}(t) \in \mathbb{C}^{(2S+1) \times (2S+1)}$  has elements

$$A(t)_{s_1, s_2} = \begin{cases} e^{j2\pi\frac{s_2}{D}t} \Delta(t) & \text{if } s_1 + s_2 = 0 \\ e^{j\pi(2\frac{s_2}{D}t - (s_1 + s_2)\mathcal{S}(t))} \frac{\sin(\pi(s_1 + s_2)\Delta(t))}{\pi(s_1 + s_2)} & \text{otherwise} \end{cases} \quad (28)$$

where  $-S \leq s_1, s_2 \leq S$ ,  $\Delta(t) = L_{\max}(t) - L_{\min}(t)$ , and  $\mathcal{S}(t) = L_{\max}(t) + L_{\min}(t)$ , with  $L_{\max}(t) = \min\left\{\frac{1}{2}; \frac{t}{D} + \frac{1}{2}\right\}$ , and  $L_{\min}(t) = \max\left\{-\frac{1}{2}; \frac{t}{D} - \frac{1}{2}\right\}$ . Similarly,  $\mathbf{A}'(t) \in \mathbb{C}^{(2S+1) \times (2S+1)}$  has elements

$$A'(t)_{s_1, s_2} = \begin{cases} e^{j2\pi\frac{s_1}{D}t} \Delta'(t) & \text{if } s_1 = s_2 \\ e^{j\pi(2\frac{s_1}{D}t + (s_2 - s_1)\mathcal{S}'(t))} \frac{\sin(\pi(s_2 - s_1)\Delta'(t))}{\pi(s_2 - s_1)} & \text{otherwise} \end{cases} \quad (29)$$

where  $-S \leq s_1, s_2 \leq S$ ,  $\Delta'(t) = L'_{\max}(t) - L'_{\min}(t)$ , and  $\mathcal{S}'(t) = L'_{\max}(t) + L'_{\min}(t)$ , with  $L'_{\max}(t) = \min\left\{\frac{1}{2}; -\frac{t}{D} + \frac{1}{2}\right\}$ , and  $L'_{\min}(t) = \max\left\{-\frac{1}{2}; -\frac{t}{D} - \frac{1}{2}\right\}$ . Detailed derivations of (25), (26), and (27) are provided in the Appendix.

### B. Trainable constellation

As done, e.g., in [18], the trainable constellation consists of a set of  $2^K$  complex numbers denoted by  $\tilde{\mathcal{C}}$ , which represent the uncentered and unnormalized constellation points. To ensure that the constraint (19c) is satisfied,  $\tilde{\mathcal{C}}$  is centered and normalized as

$$\mathcal{C} = \frac{\tilde{\mathcal{C}} - 2^{-K} \sum_{c \in \tilde{\mathcal{C}}} c}{\sqrt{2^{-K} \sum_{c \in \tilde{\mathcal{C}}} |c|^2 - \left| 2^{-K} \sum_{c \in \tilde{\mathcal{C}}} c \right|^2}}. \quad (30)$$

Although centering is not strictly necessary, it avoids a possibly unwanted direct current (DC) offset. The centered and normalized constellation  $\mathcal{C}$  is then used to modulate the data bits. Each point of  $\tilde{\mathcal{C}}$  (and  $\mathcal{C}$ ) has a predefined arbitrary bit label. By training on the BMD rate (11), optimization of the constellation geometry is performed while considering the labeling of each point. This leads to the joint optimization of the bit labeling and constellation geometry. Note that no additional complexity is introduced on the transmitter side compared to a traditional single-carrier system since it relies on BICM using the constellation  $\mathcal{C}$  (30) and pulse shaping using the filter in (23). Once the end-to-end system is trained, the learned transmit filter, constellation geometry, and corresponding labeling can simply be used *in lieu* of, e.g., an RRC filter and QAM constellation with Gray labeling.

### C. Neural network receiver

The neural receiver computes LLRs on the transmitted bits  $\mathbf{B}$  from the received samples  $\mathbf{r} \in \mathbb{C}^N$ . As shown in Fig. 3b, the neural receiver for the AWGN is a residual 1-dimensional convolutional NN [29]. For multipath channels (see Fig. 3c), an additional dense NN is needed to extract channel state information. This will be explained in more detail in Section VI-D.

The convolutional NNs are made of several ResNet blocks that have the generic architecture shown in Fig. 3a. Separable convolutional layers are used to reduce the complexity and zero-padding is employed to ensure that the output has the same length as the input. We use dilatation to increase the receptive field of the convolutional layers. As shown in Fig. 3b, the first layer is a  $\mathbb{C}2\mathbb{R}$  layer which converts the complex-valued input of length  $N$  to a 2-dimensional real-valued tensor with shape  $N \times 2$ , by stacking the real and imaginary parts. From a deep learning perspective, the second dimension serves as the “channels” of the convolutional NN. The output of the neural receiver is a two-dimensional real-valued tensor with shape  $N \times K$ , which corresponds to the LLRs of the transmitted bits  $\mathbf{B}$ .

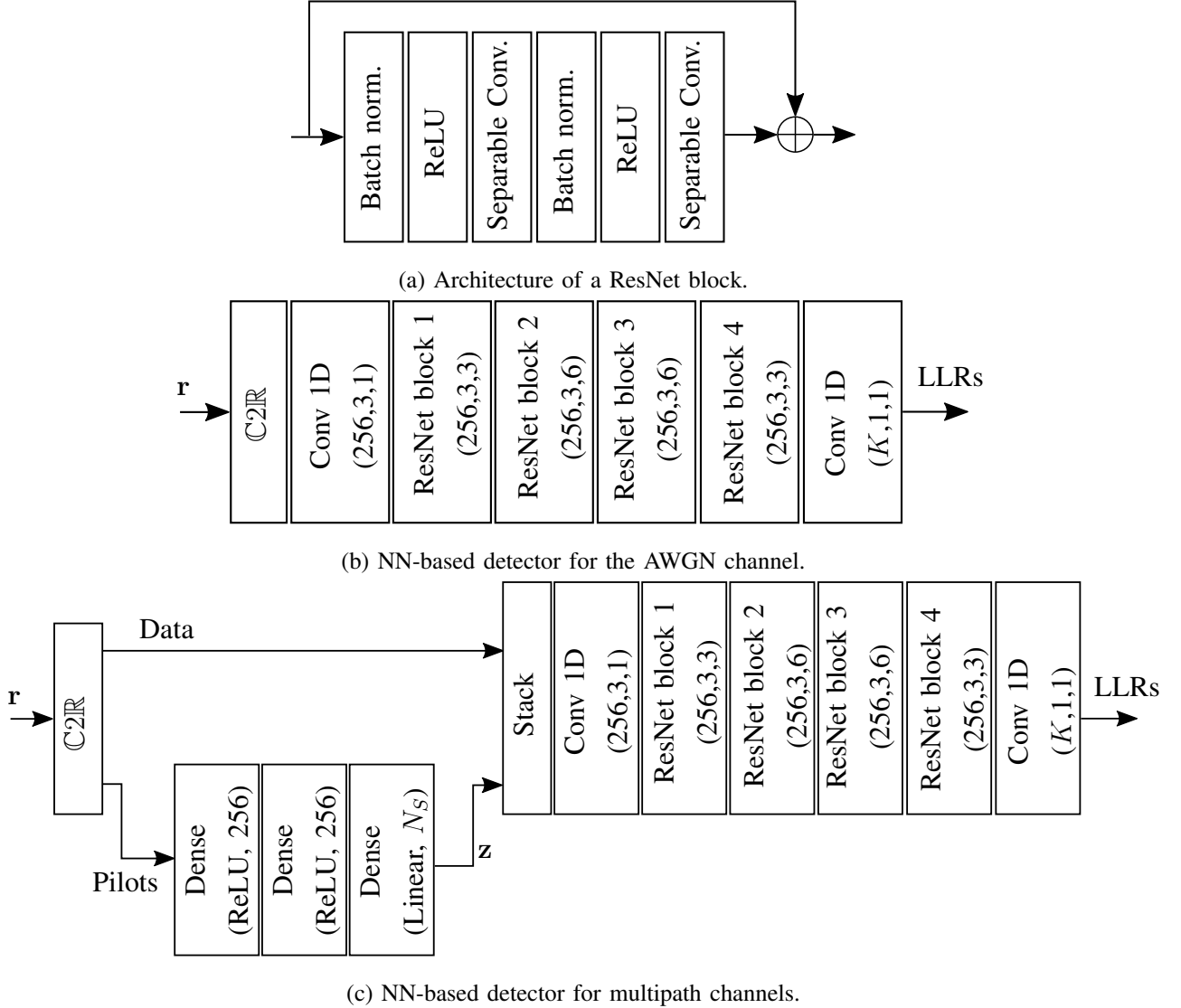


Fig. 3: Architecture of the neural receivers for the AWGN and multipath channels. For each ResNet block (dense layer), the number of kernels, kernel size, and dilatation rate (activation and number of units) are indicated.

For the multipath channel, it is assumed that the first  $N_P$  symbols of each block are pilots. As shown in Fig. 3c, these are processed by a dense NN which outputs a real-valued vector  $\mathbf{z}$  of size  $N_S$ . The vector  $\mathbf{z}$  is then stacked together with the real and imaginary parts of the received symbols  $\mathbf{r}$  along the “channels” dimension, to form a real-valued tensor with dimension  $N \times (N_S + 2)$  that serves as input to the convolutional neural receiver. This architecture was designed with the intuition that  $\mathbf{z}$  carries information on the channel state which is helpful for

computing the LLRs. We were not able to train the system without  $\mathbf{z}$  and dedicated pilots.

#### D. Training process

Training of the end-to-end system consists in jointly optimizing the transmit and receive filters, the neural receiver, the constellation as well as the corresponding bit labeling to solve (19). The maximization of the achievable rate (11) is achieved by minimizing the total binary-cross-entropy

$$\mathcal{L}(\mathcal{C}, \boldsymbol{\theta}, \boldsymbol{\psi}, \boldsymbol{\gamma}) := -\frac{1}{N} \sum_{n=0}^{N-1} \sum_{k=0}^{K-1} \mathbb{E} [\log_2 (Q_{\boldsymbol{\gamma}} (B_{n,k} | \mathbf{r})) | \mathcal{C}, \boldsymbol{\theta}, \boldsymbol{\psi}] \quad (31)$$

which is related to  $R$  by

$$\mathcal{L}(\mathcal{C}, \boldsymbol{\theta}, \boldsymbol{\psi}, \boldsymbol{\gamma}) = K - R(\mathcal{C}, \boldsymbol{\theta}, \boldsymbol{\psi}, \boldsymbol{\gamma}). \quad (32)$$

Since (31) is numerically difficult to compute, it is estimated through Monte Carlo sampling:

$$\mathcal{L}(\mathcal{C}, \boldsymbol{\theta}, \boldsymbol{\psi}, \boldsymbol{\gamma}) \approx -\frac{1}{MN} \sum_{m=0}^{M-1} \sum_{n=0}^{N-1} \sum_{k=0}^{K-1} \log_2 \left( Q_{\boldsymbol{\gamma}} \left( B_{n,k}^{[m]} | \mathbf{r}^{[m]} \right) \right) \quad (33)$$

where  $M$  is the batch size, i.e., the number of samples used to compute the estimate of  $\mathcal{L}$ , and the superscript  $[m]$  is used to refer to the  $m^{th}$  example within a batch.

Finding a local optimum of (19a) is made challenging by the constraints (19b)–(19e). The constraint (19b) is guaranteed through the normalization constant  $C(\boldsymbol{\theta})$  (25) in (23), and the constraint (19c) is achieved through the normalization of the constellation (30). Enforcing the constraint on the ACLR (19d), however, requires the computation of the in-band energy (15) as it determines the ACLR (14). With the implementation of the trainable transmit filter introduced in Section V-A, the in-band energy can be efficiently computed as

$$E_I(\boldsymbol{\theta}) = C(\boldsymbol{\theta}) \boldsymbol{\theta}^H \mathbf{E} \boldsymbol{\theta} \quad (34)$$

where  $\mathbf{E} \in \mathbb{R}^{(2S+1) \times (2S+1)}$  has elements

$$E_{s_1, s_2} = \int_{-\frac{W}{2}}^{\frac{W}{2}} \text{sinc}(Df - s_1) \text{sinc}(Df - s_2) \quad (35)$$

which can be pre-computed prior to training. This leads to

$$\text{ACLR}(\boldsymbol{\theta}) = \frac{1}{C(\boldsymbol{\theta}) \boldsymbol{\theta}^H \mathbf{E} \boldsymbol{\theta}} - 1 \quad (36)$$

when combined with (14). A derivation of (34) is provided in the Appendix.

Concerning the constraint on the PAPR (19e), we use the equivalent constraint function (20) and estimate the quantity  $V$  by Monte Carlo sampling

$$V(\boldsymbol{\theta}, \mathcal{C}, \epsilon_P) \approx \frac{1}{M'} \sum_{m=1}^{M'} \max \left( \frac{p^{[m]}(t^{[m]})}{\bar{p}} - \epsilon_P, 0 \right) \quad (37)$$

where  $M'$  is the number of samples. The signal power samples  $p^{[m]}(t^{[m]})$  are generated by sampling first random baseband symbols  $\mathbf{s}$  from the constellation  $\mathcal{C}$ , which are used to compute the time-continuous signal  $x(t)$  according to (1). The power  $p(t) = |x(t)|^2$  is then sampled at randomly chosen instants  $t^{[m]} \sim \mathcal{U}(-\frac{T}{2}, \frac{T}{2})$ .

---

**Algorithm 1** Training algorithm

---

- 1: Initialize  $\tilde{\mathcal{C}}$ ,  $\boldsymbol{\theta}$ ,  $\boldsymbol{\psi}$ ,  $\boldsymbol{\gamma}$ ,  $\eta^{[0]}$ ,  $\lambda_A^{[0]}$ , and  $\lambda_P^{[0]}$ .
- 2: **for**  $u = 0, \dots$  **do**
- 3:     Perform SGD on  $\mathcal{L}_A \left( \mathcal{C}, \boldsymbol{\theta}, \boldsymbol{\psi}, \boldsymbol{\gamma}; \lambda_A^{[u]}, \lambda_P^{[u]}, \eta^{[u]} \right)$
- 4:     ▷ Update Lagrange multipliers:
- 5:      $\lambda_A^{[u+1]} \leftarrow \lambda_A^{[u]} - \eta^{[u]} \max(\text{ACLR}(\boldsymbol{\theta}) - \epsilon_A, 0)$
- 6:      $\lambda_P^{[u+1]} \leftarrow \lambda_P^{[u]} - \eta^{[u]} V(\boldsymbol{\theta}, \mathcal{C}, \epsilon_P)$
- 7:     ▷ Update penalty parameter:
- 8:     Set  $\eta^{[u+1]}$  such that  $\eta^{[u+1]} > \eta^{[u]}$
- 9: **end for**

---

Finding a local maximum of (19) is achieved by using the augmented Lagrangian method [30, Chapter 3], which is shown in Algorithm 1 when applied to our setup. The augmented Lagrangian method consists in solving a sequence of unconstrained optimization problems (line 3), each aiming at minimizing the augmented Lagrangian

$$\begin{aligned} \mathcal{L}_A \left( \mathcal{C}, \boldsymbol{\theta}, \boldsymbol{\psi}, \boldsymbol{\gamma}; \lambda_A^{[u]}, \lambda_P^{[u]}, \eta^{[u]} \right) &:= \mathcal{L}(\mathcal{C}, \boldsymbol{\theta}, \boldsymbol{\psi}, \boldsymbol{\gamma}) - \lambda_P^{[u]} V(\boldsymbol{\theta}, \mathcal{C}, \epsilon_P) - \lambda_A^{[u]} \max(\text{ACLR}(\boldsymbol{\theta}) - \epsilon_A, 0) \\ &\quad + \frac{\eta}{2} (V(\boldsymbol{\theta}, \mathcal{C}, \epsilon_P)^2 + (\max(\text{ACLR}(\boldsymbol{\theta}) - \epsilon_A, 0))^2) \end{aligned} \quad (38)$$

where the superscript  $[u]$  refers to the  $u^{\text{th}}$  iteration,  $\lambda_A$  and  $\lambda_P$  are the Lagrange multipliers, and  $\eta$  is a positive penalty parameter that is progressively increased (line 8). At each iteration, minimizing the augmented Lagrangian is approximately achieved through SGD.

## VI. SIMULATION RESULTS

### A. Setup

The multipath channel model implemented as described in Section III was considered to train and benchmark the end-to-end learning approach. For brevity, the baseline is referred to as BL, and the end-to-end learning approach as E2E. The carrier frequency was set to 3.5 GHz and the bandwidth to  $W = 5$  MHz. The duration of the transmit and receive filters was set to  $D = 32T$  and their number of trainable parameters was set to  $S = 100$ . The block length was set to  $N = 1000$  symbols and the modulation order to 16 ( $K = 4$ ). The NN-based receiver operates on the entire block of  $N$  symbols. The signal-to-noise ratio (SNR) is defined as

$$\text{SNR} := \frac{1}{N_0}. \quad (39)$$

Training of the E2E system was carried out using the Adam optimizer [31] to perform SGD, with batches of size  $M = 10$  and a learning rate of  $10^{-3}$ . The batch size for evaluating the PAPR constraint (37) was set to  $M' = 10000$ . The penalty parameter was initialized with  $\eta^{[0]} = 10^{-2}$  and then increased according to a multiplicative schedule  $\eta^{[u+1]} = 1.003\eta^{[u]}$ . The Lagrange multipliers were both initialized with 0.

### B. AWGN channel

An AWGN channel with an SNR of 10 dB is considered in this section. More precisely, in the transfer function (2), the number of paths is set to  $P = 1$ , with  $a_0 = 1$  and  $\tau_0 = 0$ . The E2E system uses the neural receiver shown in Fig. 3b. A Gray-labeled 16QAM was used as BL with the windowed RRC filter as introduced in Section III.

Fig. 4 shows the rates  $R$  and ACLRs achieved by the BL and the E2E schemes, for different values of  $\epsilon_A$  and  $\epsilon_P$ . Concerning the BL, values of the roll-off factor  $\beta$  from the set  $\{0.0, 0.25, 0.50, 0.75, 1.0\}$  were considered. As shown in Fig 4, setting the roll-off factor to 0 gives the lowest ACLR, at the cost of a rate loss due to the ISI introduced by the windowing. Higher values of  $\beta$  lead to lower ripples which make the filter more robust to windowing, at the cost of higher ACLR. Concerning the E2E approach, values of  $\epsilon_A$  from the set  $\{-50, -40, -30, -20\}$  dB were considered, and are indicated in Fig. 4 only for the plot corresponding to  $\epsilon_P = 4$  dB for clarity. As one can see, the ACLR incurred by the E2E system is always lower or very close to the value of  $\epsilon_A$  for which it was trained. This indicates that

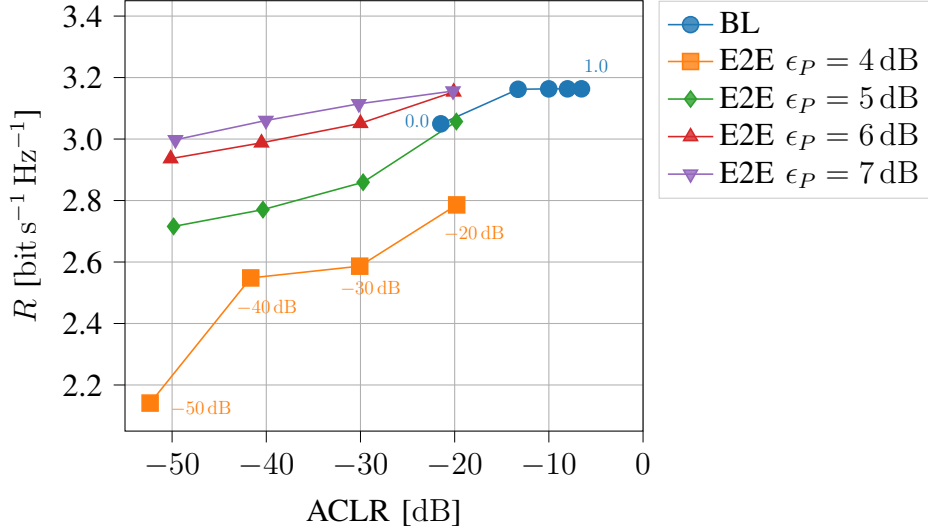


Fig. 4: Rates and ACLR achieved by the BL and E2E systems. The different points for the BL (from left to right) are obtained by having the roll-off factor  $\beta$  take values from the set  $\{0.0, 0.25, 0.50, 0.75, 1.0\}$ . For the E2E system, values of  $\epsilon_A$  from the set  $\{-50, -40, -30, -20\}$  dB (from left to right) were considered. These are only indicated for  $\epsilon_P = 4.0$  dB for clarity.

the training process allows accurate control of the ACLR through this parameter. Moreover, it enables ACLRs up to 30 dB lower than the ones of the BL, without significant rate loss.

The PAPR constraint has the strongest impact on the rate. To quantify the impact of the PAPR constraint on the power distribution, Fig. 5 shows the complementary cumulative distribution function (CCDF) of the normalized power for  $\epsilon_A = 10$  dB. As one can see, constraining the PAPR has the expected impact on the power distribution, as it significantly reduces the occurrences of power peaks, at the cost of a rate loss (Fig. 4). The E2E system achieves the lowest power peaks when  $\epsilon_P = 4$  dB, whereas setting  $\epsilon_P$  to 7 dB leads to the same CCDF as for a windowed sinc filter ( $\beta = 0$ ). Concerning the power spectrum, Fig. 6 shows the PSDs of the learned filters ( $\epsilon_P = 6$  dB) and that of the baseline ( $\beta = 0$ ). The learned filters emit less in the adjacent bands and the power floor depends on the constraint value  $\epsilon_A$ .

To get some more insight into the E2E system, we show in Fig. 7 and Fig. 8 the learned constellations and transmit filters, respectively, for different values of  $\epsilon_A$  and  $\epsilon_P$ . As one can see from Fig. 7, a form of Gray labeling is always learned jointly with the constellation geometry. When strongly constraining both the ACLR and PAPR (bottom left), a phase-shift keying (PSK)

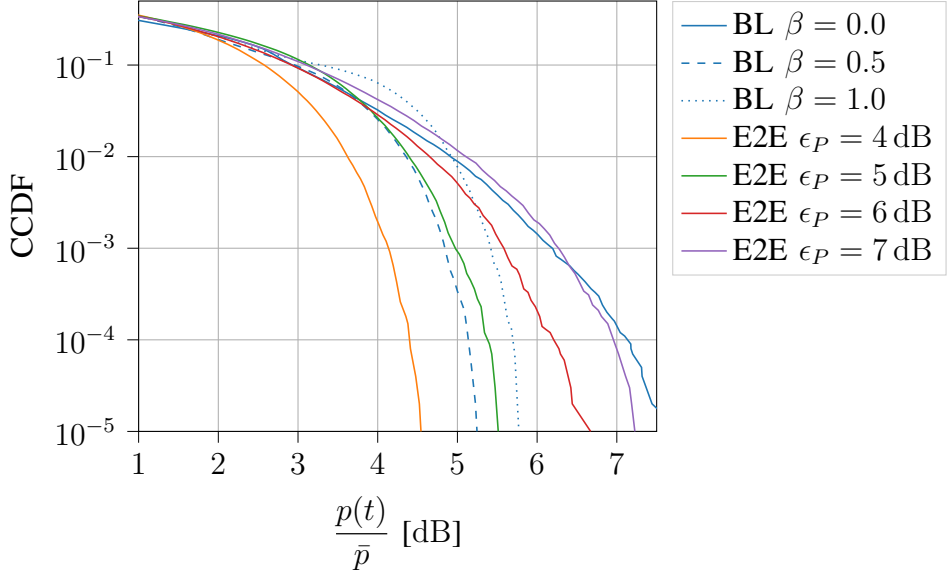


Fig. 5: CCDF of the normalized power of the BL and E2E system for  $\epsilon_A = -30$  dB.

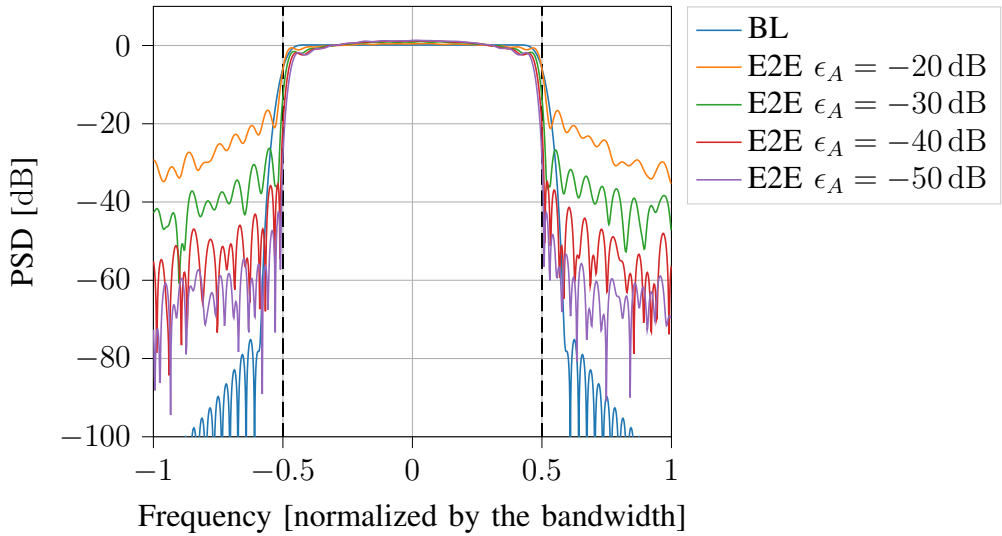


Fig. 6: PSDs of the baseline ( $\beta = 0$ ) and the E2E system for  $\epsilon_P = 6$  dB.

constellation is learned and points are clustered by groups of two which differ only in a single bit. This means that the E2E system is willingly “sacrificing” a bit of information to improve the PAPR. Lowering either of the constraints leads to constellations with two levels of amplitudes. The softest constraints (top row) lead to the least intuitive geometries. Overall, as expected, it seems that the constellations are mainly determined by the PAPR and not the ACLR constraint.

Interpreting the learned transmit filters in Fig. 8 is less straightforward. The learned filters have

some similarity with an RRC filter, especially when both constraints are strong (bottom left). In this case, the imaginary component vanishes, similar to conventional filters that have only a real component. However, relaxing the constraints leads to significant imaginary components. Moreover, the pulse shape is not symmetric around the peak in contrast to conventional filters. In contrast to the constellation geometry, which is mainly determined by the PAPR constraint, the pulse shape is—a bit unexpectedly—impacted by both constraints.

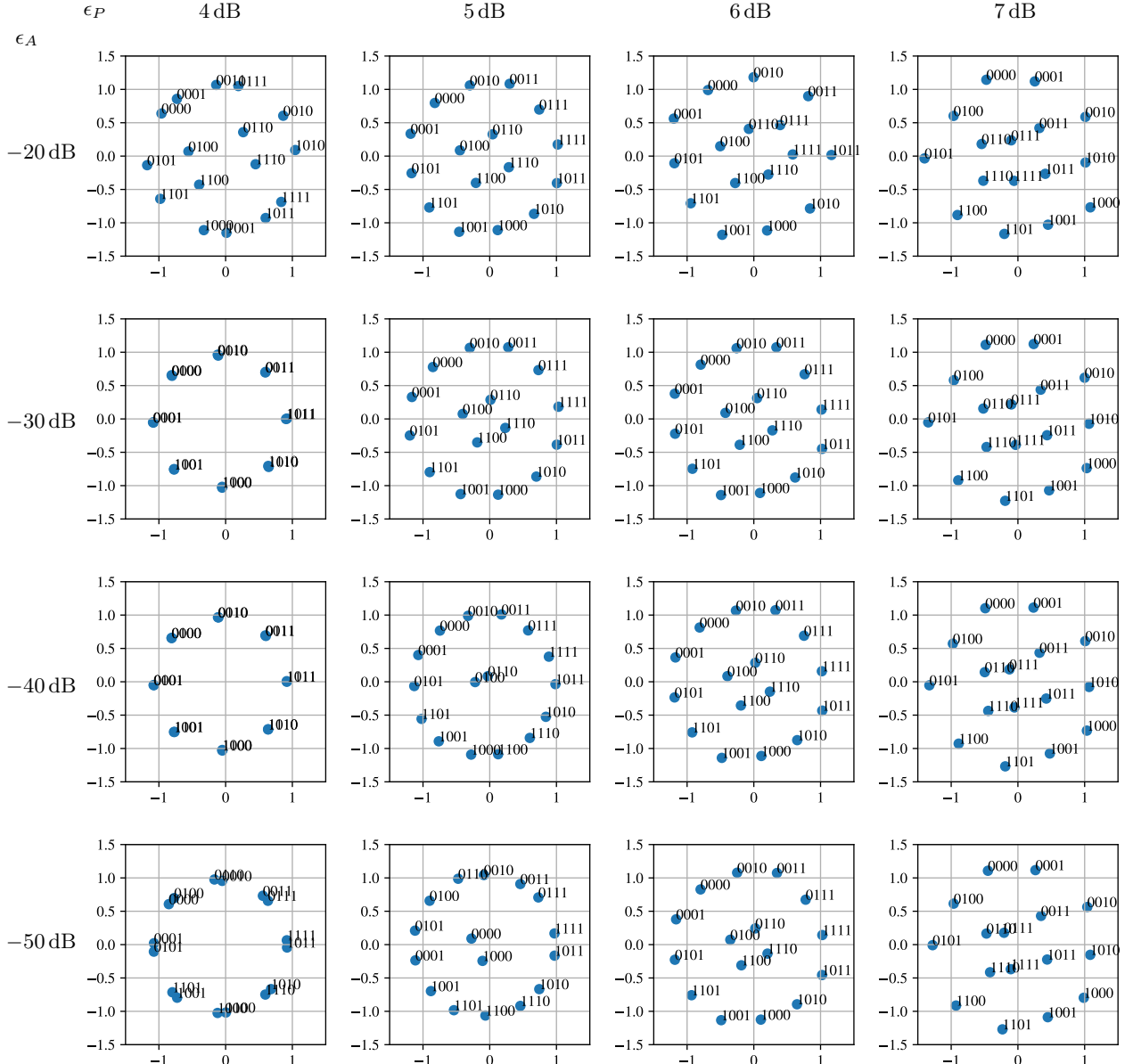


Fig. 7: Learned constellation geometries and bit labels for different values of  $\epsilon_A$  and  $\epsilon_P$ .

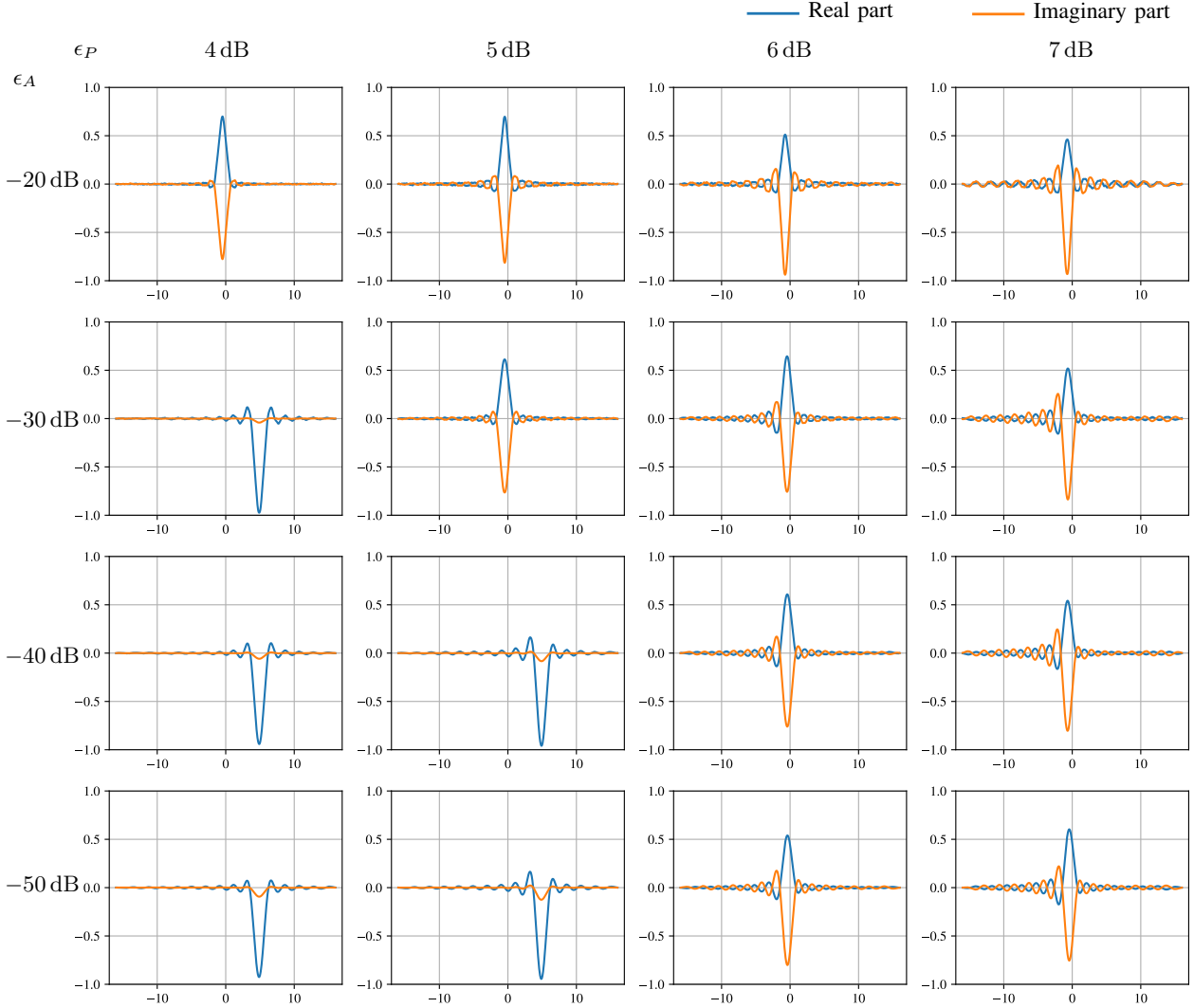


Fig. 8: Learned transmit filters for different values of  $\epsilon_A$  and  $\epsilon_P$ .

### C. Multiple access channel

User multiplexing is typically achieved through OMA in the time, frequency, code, or spatial domains. For example, different users would share the available spectrum by transmitting only on dedicated bands, using the ACLR as a measure of the power a user leaks onto the adjacent bands used by the other users. It is well-known that such OMA approaches are sub-optimal and a significant research effort is dedicated to the design of non-orthogonal multiple access (NOMA) schemes [32]. In this section, we explore how the use of dedicated constellation geometries and transmit filters could enable multiplexing. An AWGN channel with SNR set to 10 dB is considered, as in Section VI-B. However, we now consider two interfering users as illustrated

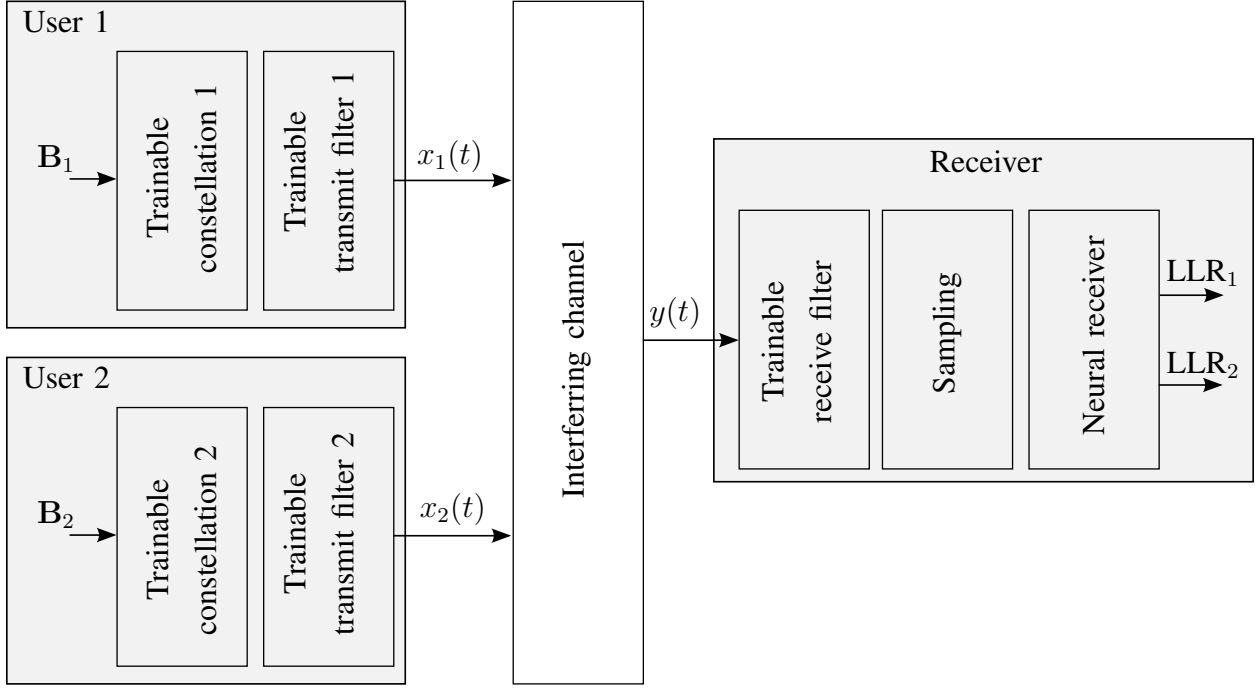


Fig. 9: End-to-end system with two interfering users, each with a trainable transmit filter and constellation, and a receiver with a trainable receive filter and NN.

in Fig. 9. The two users transmit with the same average power and over the same band. Each user has a dedicated trainable constellation geometry, bit labeling, and transmit filter, as shown in Fig. 9. The receiver includes a trainable receive filter and neural receiver, that are jointly optimized together with the two trainable transmitters over the interfering channel.

Training is done on the sum-log rate

$$\mathcal{R} := w \log_2 (R_1) + (1 - w) \log_2 (R_2) \quad (40)$$

where  $R_1$  and  $R_2$  are the achievable BMD rates (11) for user 1 and user 2, respectively, and  $w \in (0, 1)$  allows favoring one user over the other. Intuitively, by using the sum-log rate, increasing the rate of the user with the highest rate leads to less reward than increasing the rate of the user with the lowest rate, thus favoring fairness. Formally, the sum-log rate is closely related to proportionality fairness [33]. A rate allocation  $(r_1, r_2)$  is said to be proportionally fair if for any other allocation  $(r'_1, r'_2)$ , one has

$$w \frac{r'_1 - r_1}{r_1} + (1 - w) \frac{r'_2 - r_2}{r_2} \leq 0. \quad (41)$$

Especially, when  $w = 0.5$ , increasing the rate of one user by  $p\%$  can only be achieved by reducing the rate of the other user by at least  $p\%$ . Except for the different loss function, training of the end-to-end system was achieved using the method depicted in Section V-D, with  $\epsilon_A$  set to  $-30$  dB and  $\epsilon_P$  set to  $6$  dB. The two users are subject to the same PAPR and ACLR constraints. The latter enforces them explicitly to operate on the same band.

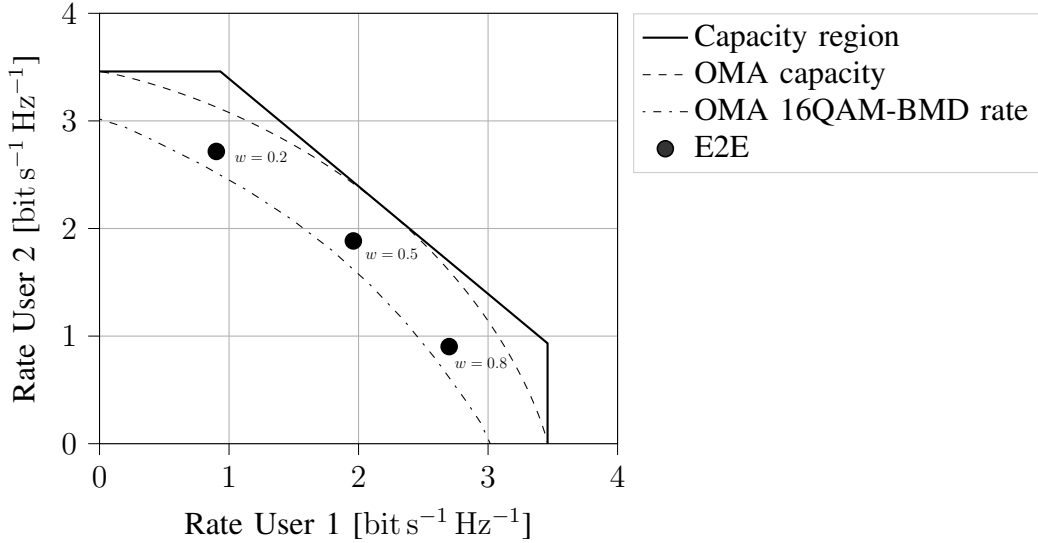


Fig. 10: Achievable rates for the two interfering users, with  $\epsilon_A = -30$  dB and  $\epsilon_P = 6$  dB.

Fig. 10 shows the rates achieved by the two users. This figure also shows the capacity region and the OMA capacity, both achieved by Gaussian modulation and an optimal non-BMD receiver, making these rates unachievable by practical systems. For comparison, we also show the achievable rate of OMA with 16QAM and an BMD receiver. As one can see, the E2E system outperforms the rates enabled by the latter for the three considered values of  $w$ . The highest ACLR achieved by the E2E system is  $-29.95$  dB and the CCDF of the PAPR at  $5.60$  dB is  $10^{-3}$ , showing that the constraints have the expected impact on the learned waveforms.

To better understand how the E2E system operates, we show in Fig. 11 and Fig. 12, respectively, the learned constellations and filters for  $w = 0.5$ . As one can see, the constellations are along close-to orthogonal axes. Moreover, the learned transmit filters are also only partially overlapping, as each user favors a distinct part of the available band. An in-depth study of the learned filters and constellations is out of scope of this paper and left for future investigation.

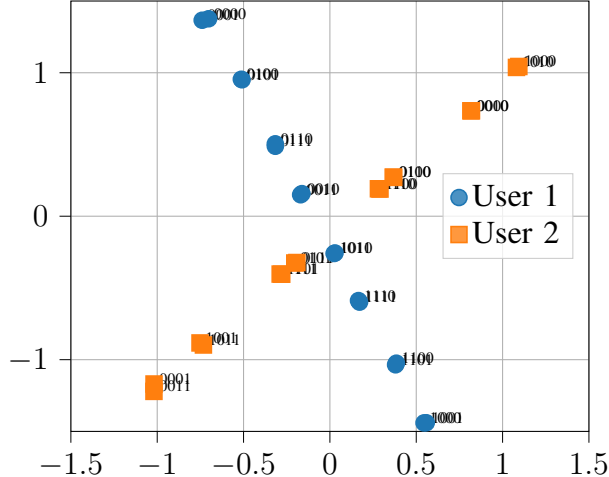


Fig. 11: Learned constellations for two interfering users ( $w = 0.5$ ,  $\epsilon_A = -30$  dB,  $\epsilon_P = 6$  dB).

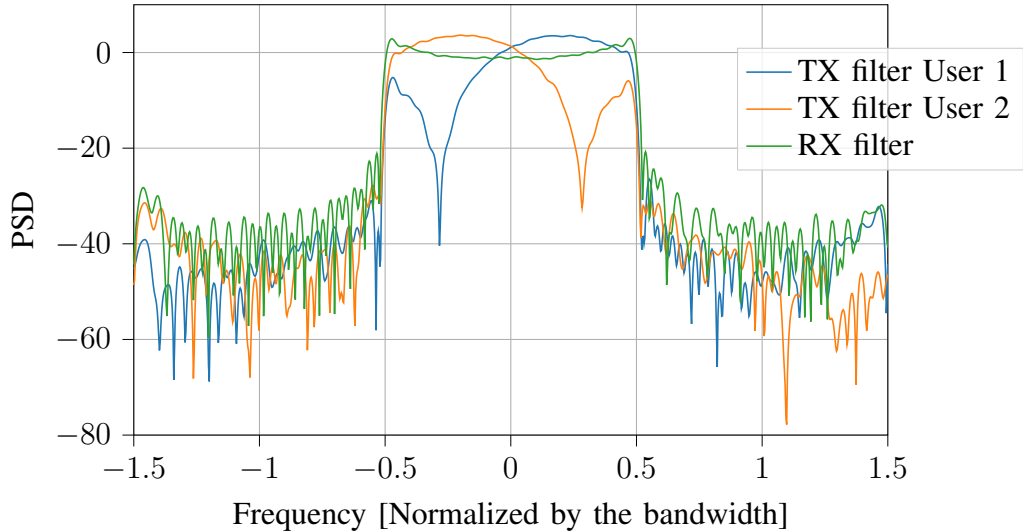


Fig. 12: The two transmit filters and single receive filter learned over the interference channel, with  $w = 0.5$ ,  $\epsilon_A = -30$  dB, and  $\epsilon_P = 6$  dB.

#### D. Multipath channel

The use of multi-carrier waveforms, such as OFDM, for multipath channels has been mainly motivated by the low-complexity single-tap equalization they enable. However, with the advent of neural receivers that can be efficiently implemented on dedicated hardware [34], this advantage might become less relevant, especially as multi-carrier waveforms are well-known to incur high PAPRs, leading to power amplifier inefficiencies.

In order to illustrate this, we consider a multipath channel in this section. We simulate the channel according to the 3GPP 38.901 UMi line-of-sight (LoS) and non-line-of-sight (NLoS) models, based on a dataset of baseband channel coefficients  $a_p$  and corresponding delays  $\tau_p$  which were generated with the help of the Quadriga channel simulator [35]. The channel is assumed to be static for the duration of a block, corresponding to a low-mobility scenario. Training and benchmarking were performed on two different datasets to ensure that the E2E system is able to generalize to previously unseen channel realizations. Although over-the-air training using the technique described in [36] might be possible, we believe that our approach is most practical if training is done offline, prior to deployment.

An OFDM waveform with Gray-labeled 16QAM, LMMSE channel estimation, and single-tap equalization was implemented to serve as BL, with a subcarrier spacing of 30 kHz and 166 subcarriers. Each block consists of one slot, i.e., 14 OFDM symbols. A standard 5G New Radio (5G NR) pilot pattern was used, with an overhead of 1/14 ( $\approx 7.14\%$ ).

For the E2E system, the neural receiver from Fig. 3c was used. The first  $N_P = 32$  samples of each block were used as trainable pilots, which were centered and normalized as for the constellation. The length of the vector  $\mathbf{z}$  in Fig. 3c, which is generated by the dense network from the received pilot symbols, was set to  $N_S = 64$ . Training was done over the range of SNRs from 5 dB to 20 dB, i.e., the SNR was randomly sampled for each training example.

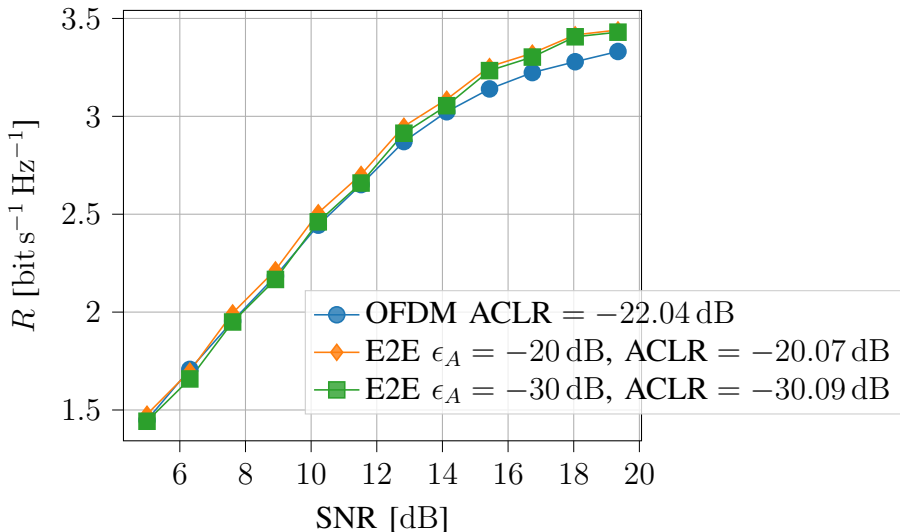


Fig. 13: Rates achieved by the OFDM BL and the two E2E systems trained with different ACLR constraints and  $\epsilon_P = 7$  dB. The ACLR achieved by each waveform is indicated in the legend.

Fig. 13 shows the rates achieved by the BL and the E2E system for  $\epsilon_P$  set to 7 dB and  $\epsilon_A$  to  $-20$  dB and  $-30$  dB. The ACLR achieved by each waveform is indicated in the legend. The E2E system achieves rates competitive or higher than the ones of the BL, especially at high SNRs. This is particularly interesting for  $\epsilon_A = -30$  dB, where the E2E system enables an ACLR that is 10 dB lower than that of the BL. Regarding the PAPR, Fig. 14 shows the CCDF of the normalized power distribution of the compared waveforms. As one can see, the E2E system achieves a 2 dB gain over OFDM for a CCDF value of  $10^{-4}$ .

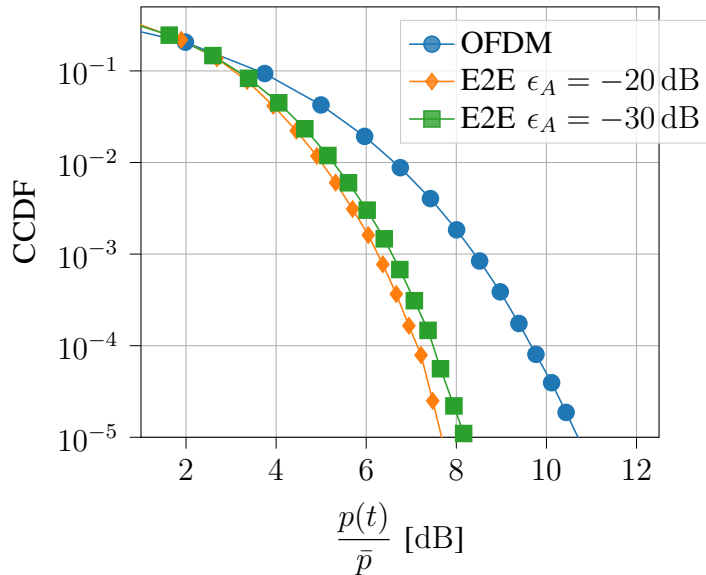


Fig. 14: Power distribution of OFDM and two E2E systems trained with different ACLR constraints and  $\epsilon_P = 7$  dB.

Fig. 15 shows the learned constellation, corresponding labeling, and transmit filter for  $\epsilon_A = -30$  dB and  $\epsilon_P = 7$  dB. One can see that the E2E system has learned a Gray labeled 16QAM constellation. Interpreting the learned transmit filter is more difficult and left to future work. One can notice that it has similarities with a conventional RRC filter, e.g., the presence of a central peak and adjacent ripples, but differs through the presence of a real and imaginary component and the lack of symmetry around the peak.

## VII. CONCLUSION

We have introduced a new method for designing single-carrier waveforms for communication systems through joint optimization of the transmit filter, receive filter, constellation geometry,

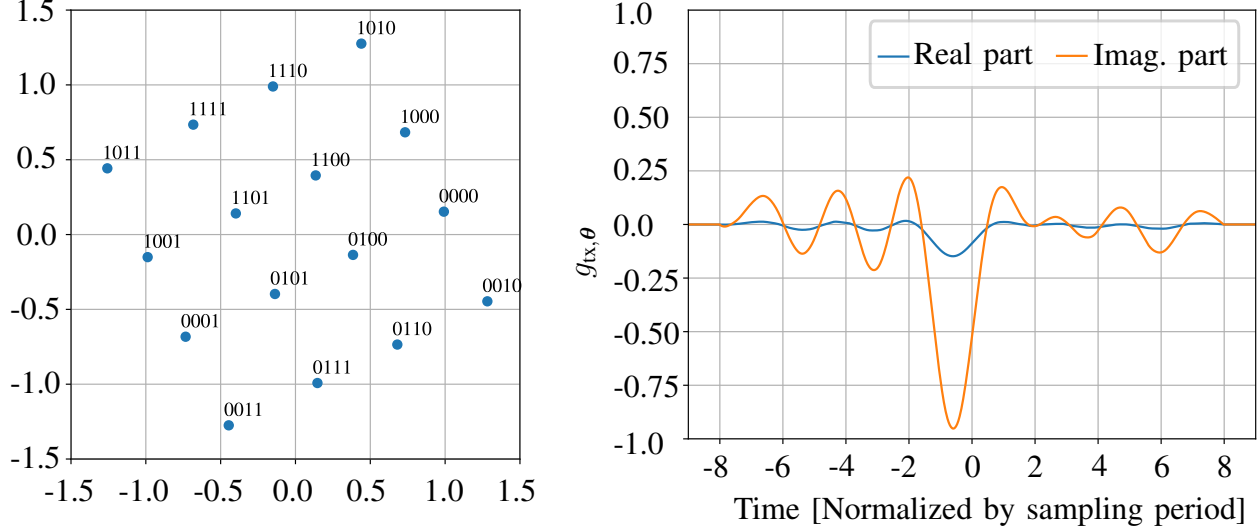


Fig. 15: Learned constellation, corresponding bit labeling, and transmit filter for the multipath channel with  $\epsilon_A = -30$  dB and  $\epsilon_P = 7$  dB.

corresponding bit labeling, and a neural receiver. The training process was formulated as an optimization problem with constraints on the ACLR and PAPR, where the objective function is an achievable rate of practical systems using BMD receivers. Our results show that the proposed method enables fine control of the tradeoff between the information rate, ACLR, and PAPR. On the AWGN channel, the learned waveforms achieve rates that are competitive with the ones of conventional waveforms, but with significantly lower ACLRs. Lower PAPRs are also possible, however at the cost of a rate loss. We have further illustrated how the proposed method could enable a new approach for multiplexing of multiple users through the joint optimization of constellation geometries and transmit filters. We have also shown that the learned single-carrier waveforms are competitive with OFDM for multipath channels. They enable similar or higher rates, but with significantly lower PAPRs and ACLRs. The interpretation of the learned filters reminds an open problem that requires future investigation. Key directions of future investigation include the extension to other channel models (e.g., optical, sub-THz, MIMO), new use cases (e.g., faster-than-Nyquist signaling), as well as prototyping with software-defined radios.

## APPENDIX

### A. Derivation of (25)

The transmit filter is described in the time domain as

$$g_{\text{tx},\theta}(t) = \frac{\sqrt{C(\theta)}}{D} \text{rect}\left(\frac{t}{D}\right) \sum_{s=-S}^S \theta_s e^{j2\pi \frac{s}{D} t}. \quad (42)$$

Its total energy can be computed as

$$E_T(\theta) = \int_{-\frac{D}{2}}^{\frac{D}{2}} |g_{\text{tx},\theta}(t)|^2 dt = \frac{C(\theta)}{D^2} \sum_{s_1=-S}^S \sum_{s_2=-S}^S \theta_{s_1} \theta_{s_2}^* \int_{-\frac{D}{2}}^{\frac{D}{2}} e^{j\frac{2\pi}{D}(s_1-s_2)t} dt. \quad (43)$$

The integral of the last equation is

$$\int_{-\frac{D}{2}}^{\frac{D}{2}} e^{j\frac{2\pi}{D}(s_1-s_2)t} dt = \begin{cases} 0, & \text{if } s_1 \neq s_2 \\ D, & \text{if } s_1 = s_2 \end{cases} \quad (44)$$

which leads to

$$E_T(\theta) = \frac{C(\theta)}{D} \theta^H \theta. \quad (45)$$

To ensure that the transmit filter has unit energy, the normalization constant is hence set to

$$C(\theta) = \frac{D}{\theta^H \theta}. \quad (46)$$

### B. Derivation of (26)

One has

$$(g_{\text{tx},\theta} * g_{\text{rx},\psi}^*) (t) = \int g_{\text{tx},\theta}(w) g_{\text{rx},\psi}^*(t-w) dw \quad (47)$$

$$= \frac{\sqrt{C(\theta)}}{D^2} \sum_{s_1=-S}^S \sum_{s_2=-S}^S \psi_{s_1}^* \theta_{s_2} \int_{-\frac{D}{2}}^{\frac{D}{2}} \text{rect}\left(\frac{t-w}{D}\right) e^{j\frac{2\pi}{D}(s_2 w - (t-w)s_1)} dw \quad (48)$$

which equals 0 if  $t \notin (-D, D)$ . Assuming  $t \in (-D, D)$ , let us define  $z := \frac{t-w}{D}$ . Then

$$(g_{\text{tx},\theta} * g_{\text{rx},\psi}^*) (t) = \frac{\sqrt{C(\theta)}}{D} \sum_{s_1=-S}^S \sum_{s_2=-S}^S \psi_{s_1}^* \theta_{s_2} e^{j2\pi \frac{s_2}{D} t} \int_{\frac{t}{D} - \frac{1}{2}}^{\frac{t}{D} + \frac{1}{2}} \text{rect}(z) e^{-j2\pi(s_1+s_2)z} dz. \quad (49)$$

By introducing  $I_{\min}(t) := \max\left(-\frac{1}{2}; \frac{t}{D} - \frac{1}{2}\right)$  and  $I_{\max}(t) := \min\left(\frac{1}{2}; \frac{t}{D} + \frac{1}{2}\right)$ , one has

$$(g_{\text{tx},\theta} * g_{\text{rx},\psi}^*) (t) = \frac{\sqrt{C(\theta)}}{D} \sum_{s_1=-S}^S \sum_{s_2=-S}^S \psi_{s_1}^* \theta_{s_2} e^{j2\pi \frac{s_2}{D} t} \int_{I_{\min}(t)}^{I_{\max}(t)} e^{-j2\pi(s_1+s_2)z} dz \quad (50)$$

$$= \frac{\sqrt{C(\theta)}}{D} \theta^T \mathbf{A}(t) \psi \quad (51)$$

where  $\mathbf{A}(t)$  is a  $(2S + 1) \times (2S + 1)$  complex-valued matrix such that

$$A(t)_{s_1, s_2} = e^{j2\pi \frac{s_2}{D} t} \int_{I_{\min}(t)}^{I_{\max}(t)} e^{-j2\pi(s_1 + s_2)z} dz \quad (52)$$

$$= \begin{cases} e^{j2\pi \frac{s_2}{D} t} \Delta(t) & \text{if } s_1 + s_2 = 0 \\ e^{j\pi(2\frac{s_2}{D} t - (s_1 + s_2)\mathcal{S}(t))} \frac{\sin(\pi(s_1 + s_2)\Delta(t))}{\pi(s_1 + s_2)} & \text{otherwise} \end{cases} \quad (53)$$

and  $\Delta(t) := I_{\max}(t) - I_{\min}(t)$ ,  $\mathcal{S}(t) := I_{\max}(t) + I_{\min}(t)$ .

### C. Derivation of (27)

The derivation follows the same steps as that of (26) and is not shown for brevity.

### D. Derivation of (34)

The in-band energy of the transmitted signal is

$$E_I(\boldsymbol{\theta}) = \int_{-\frac{W}{2}}^{\frac{W}{2}} |\hat{g}_{\text{tx}, \boldsymbol{\theta}}(f)|^2 df \quad (54)$$

$$= C(\boldsymbol{\theta}) \sum_{s_1=-S}^S \sum_{s_2=-S}^S \theta_{s_1}^* \theta_{s_2} \int_{-\frac{W}{2}}^{\frac{W}{2}} \text{sinc}(Df - s_1) \text{sinc}(Df - s_2) df \quad (55)$$

$$= C(\boldsymbol{\theta}) \boldsymbol{\theta}^H \mathbf{E} \boldsymbol{\theta} \quad (56)$$

where  $\mathbf{E}$  is the real-valued  $(2S + 1) \times (2S + 1)$  matrix with elements

$$E_{s_1, s_2} = \int_{-\frac{W}{2}}^{\frac{W}{2}} \text{sinc}(Df - s_1) \text{sinc}(Df - s_2) df \quad (57)$$

which can be easily pre-computed for a given bandwidth  $W$  and filter duration  $D$ .

## REFERENCES

- [1] F. Ait Aoudia and J. Hoydis, “End-to-end Waveform Learning Through Joint Optimization of Pulse and Constellation Shaping,” *preprint arXiv:2106.15158*, 2021.
- [2] O. Tervo, T. Levanen, K. Pajukoski, J. Hulkko, P. Wainio, and M. Valkama, “5G New Radio Evolution Towards Sub-THz Communications,” in *2nd 6G Wireless Summit (6G SUMMIT)*, 2020, pp. 1–6.
- [3] R. Hadani, S. Rakib, M. Tsatsanis, A. Monk, A. J. Goldsmith, A. F. Molisch, and R. Calderbank, “Orthogonal Time Frequency Space Modulation,” in *IEEE Wireless Commun. and Netw. Conf. (WCNC)*, 2017, pp. 1–6.
- [4] G. Fettweis, M. Krondorf, and S. Bittner, “GFDM - Generalized Frequency Division Multiplexing,” in *IEEE 69th Veh. Technol. Conf. (VTC Spring)*, 2009, pp. 1–4.
- [5] B. Krongold and D. Jones, “An Active-Set Approach for OFDM PAR Reduction via Tone Reservation,” *IEEE Trans. Signal Processing*, vol. 52, no. 2, pp. 495–509, 2004.

- [6] G. Wunder, R. F. Fischer, H. Boche, S. Litsyn, and J.-S. No, “The PAPR Problem in OFDM Transmission: New Directions for a Long-Lasting Problem,” *IEEE Signal Process. Mag.*, vol. 30, no. 6, pp. 130–144, 2013.
- [7] H. Ye, G. Y. Li, and B.-H. Juang, “Power of Deep Learning for Channel Estimation and Signal Detection in OFDM Systems,” *IEEE Wireless Commun. Lett.*, vol. 7, no. 1, pp. 114–117, 2018.
- [8] N. Shlezinger, N. Farsad, Y. C. Eldar, and A. J. Goldsmith, “ViterbiNet: A Deep Learning Based Viterbi Algorithm for Symbol Detection,” *IEEE Trans. Wireless Commun.*, vol. 19, no. 5, pp. 3319–3331, 2020.
- [9] M. Honkala, D. Korpi, and J. M. J. Huttunen, “DeepRx: Fully Convolutional Deep Learning Receiver,” *IEEE Trans. Wireless Commun.*, vol. 20, no. 6, pp. 3925–3940, 2021.
- [10] T. O’Shea and J. Hoydis, “An Introduction to Deep Learning for the Physical Layer,” *IEEE Trans. Cogn. Commun. Netw.*, vol. 3, no. 4, pp. 563–575, Dec. 2017.
- [11] G. Caire, G. Taricco, and E. Biglieri, “Bit-Interleaved Coded Modulation,” *IEEE Trans. Inform. Theory*, vol. 44, no. 3, pp. 927–946, May 1998.
- [12] H. Tataria, M. Shafi, A. F. Molisch, M. Dohler, H. Sjöland, and F. Tufvesson, “6G Wireless Systems: Vision, Requirements, Challenges, Insights, and Opportunities,” *Proceedings of the IEEE*, vol. 109, no. 7, pp. 1166–1199, 2021.
- [13] L. Li, C. Tellambura, and X. Tang, “Improved Tone Reservation Method Based on Deep Learning for PAPR Reduction in OFDM System,” in *11th Int. Conf. on Wireless Commun. and Signal Process. (WCSP)*, 2019, pp. 1–6.
- [14] X. Wang, N. Jin, and J. Wei, “A Model-Driven Deep Learning Algorithm for PAPR Reduction in OFDM System,” *IEEE Commun. Lett.*, pp. 1–1, 2021.
- [15] B. Wang, Q. Si, and M. Jin, “A Novel Tone Reservation Scheme Based on Deep Learning for PAPR Reduction in OFDM Systems,” *IEEE Commun. Lett.*, vol. 24, no. 6, pp. 1271–1274, 2020.
- [16] B. Krongold and D. Jones, “PAR reduction in OFDM via active constellation extension,” *IEEE Trans. Broadcast.*, vol. 49, no. 3, pp. 258–268, 2003.
- [17] M. Zhang, M. Liu, and Z. Zhong, “Neural Network Assisted Active Constellation Extension for PAPR Reduction of OFDM System,” in *11th Int. Conf. on Wireless Commun. and Signal Processing (WCSP)*, 2019, pp. 1–6.
- [18] F. Ait Aoudia and J. Hoydis, “End-to-end Learning for OFDM: From Neural Receivers to Pilotless Communication,” *IEEE Trans. Wireless Commun.*, pp. 1–1, 2021.
- [19] ———, “Trimming the Fat from OFDM: Pilot- and CP-less Communication with End-to-end Learning,” in *IEEE Int. Conf. on Commun. Workshops (ICC Workshops)*, 2021, pp. 1–6.
- [20] T. V. Luong, Y. Ko, M. Matthaiou, N. A. Vien, M.-T. Le, and V.-D. Ngo, “Deep Learning-Aided Multicarrier Systems,” *IEEE Trans. Wireless Commun.*, vol. 20, no. 3, pp. 2109–2119, 2021.
- [21] M. Kim, W. Lee, and D.-H. Cho, “A Novel PAPR Reduction Scheme for OFDM System Based on Deep Learning,” *IEEE Commun. Lett.*, vol. 22, no. 3, pp. 510–513, 2018.
- [22] M. Goutay, F. Ait Aoudia, J. Hoydis, and J.-M. Gorce, “End-to-End Learning of OFDM Waveforms with PAPR and ACLR Constraints,” *preprint arXiv:2106.16039*, 2021.
- [23] L. Shi, X. Zhang, W. Wang, Z. Wang, A. Vladimirescu, Y. Zhang, and J. Wang, “PAPR reduction based on deep autoencoder for VLC DCO-OFDM system,” in *IEEE Int. Symp. on Broadband Multimedia Syst. and Broadcast. (BMSB)*, 2019, pp. 1–4.
- [24] L. Hao, D. Wang, Y. Tao, W. Cheng, J. Li, and Z. Liu, “The Extended SLM Combined Autoencoder of the PAPR Reduction Scheme in DCO-OFDM Systems,” *Appl. Sci.*, vol. 9, no. 5, 2019.
- [25] J. Song, C. Häger, J. Schröder, H. Wymeersch *et al.*, “End-to-end Autoencoder for Superchannel Transceivers with Hardware Impairment,” *preprint arXiv:2103.15856*, 2021.

- [26] J. G. Proakis, M. Salehi, N. Zhou, and X. Li, *Communication Systems Engineering*. Prentice Hall New Jersey, 1994, vol. 2.
- [27] G. Böcherer, “Achievable Rates for Probabilistic Shaping,” *preprint arXiv:1707.01134*, 2017.
- [28] S. Cammerer, F. Ait Aoudia, S. Dörner, M. Stark, J. Hoydis, and S. ten Brink, “Trainable Communication Systems: Concepts and Prototype,” *IEEE Trans. Commun.*, vol. 68, no. 9, pp. 5489–5503, 2020.
- [29] K. He, X. Zhang, S. Ren, and J. Sun, “Deep Residual Learning for Image Recognition,” in *Proc. IEEE Conf. on Comput. Vision and Pattern Recognit. (CVPR)*, June 2016.
- [30] D. P. Bertsekas, *Constrained optimization and Lagrange multiplier methods*. Academic press, 2014.
- [31] D. P. Kingma and J. Ba, “Adam: A Method for Stochastic Optimization,” in *Proc. of the 3rd Int. Conf. on Learn. Representations (ICLR)*, 2014.
- [32] B. Makki, K. Chitti, A. Behravan, and M.-S. Alouini, “A Survey of NOMA: Current Status and Open Research Challenges,” *IEEE Open J. of the Commun. Soc.*, vol. 1, pp. 179–189, 2020.
- [33] F. Kelly, “Charging and Rate Control for Elastic Traffic,” *Eur. Trans. on Telecommun.*, vol. 8, no. 1, pp. 33–37, 1997.
- [34] W. J. Dally, Y. Turakhia, and S. Han, “Domain-Specific Hardware Accelerators,” *Commun. ACM*, vol. 63, no. 7, p. 48–57, June 2020.
- [35] “QuaDRiGa,” <https://quadriga-channel-model.de/>, Accessed: 2021-01-07.
- [36] F. Ait Aoudia and J. Hoydis, “Model-free Training of End-to-end Communication Systems,” *IEEE J. Sel. Areas Commun.*, vol. 37, no. 11, pp. 2503–2516, 2019.